ARTICLE

Nickel-substituted $Ba_{0.5}Sr_{0.5}Co_{0.8}Fe_{0.2}O_{3-\delta}$: a highly active perovskite oxygen electrode for reduced-temperature solid oxide fuel cells

Lu Li,[a] Hua Yang,[a] Zhenghui Gao,[a] Feifei Dong,*[a] Guangming Yang,[c] Meng Ni [b] and Zhan Lin *[a]

A key need for the advancement of high-performance solid oxide fuel cells (SOFCs) is to develop viable cathode materials with high electrocatalytic activity for oxygen reduction reaction (ORR) at reduced operating temperatures below 700 °C. Here, we report a Ni-substituted perovskite composition $Ba_{0.5}Sr_{0.5}Co_{0.7}Fe_{0.2}Ni_{0.1}O_{3-\delta}$ (BSCFN) as a potential cathode material focusing on enhancing electrochemical performance. Considerable attention is paid to the research of physicochemical properties primarily by crystal structure and oxygen transport measurements, with the aim to build up the correlation with the ORR activity. With the BSCFN cathode, a symmetrical cell achieves a very low area-specific polarization resistance of only ~0.018 Ω cm^2 and a single cell delivers a maximum power density as high as ~1.8 W cm^{-2} at 650 °C. Such large electrode performance improvement is attributed to sustained cubic-symmetry perovskite structure and fast oxygen kinetics as promoted by Ni substitution. The desirable ORR activity and durability highlight the potential of BSCFN as a highly promising oxygen electrode for reduced-temperature SOFCs.

Introduction

Solid oxide fuel cells (SOFCs) are widely recognized as clean and efficient energy devices that enable direct electrochemical conversion of a variety of chemical fuels into electrical power.[1-3] Over an extended period, the principal obstacles to commercialization of SOFCs are the high processing and operating costs associated with the high operating temperatures (typically 700-1000 °C). To facilitate the utilization of low-cost manufacturing materials and the improvement of long-term durability of SOFCs, tremendous efforts have been devoted to lowering the operating temperature, with this being a central goal of current research.[4,5] However, a universal challenge for developing high-performance low-temperature SOFCs (LT-SOFCs) arises from the polarization losses of electrodes, especially the notoriously sluggish kinetics of the oxygen reduction reaction (ORR) on the cathodes at reduced temperatures. Therefore, considerable research activities have been carried out to explore electrocatalysts with high catalytic activity for ORR.[6-9]

Promising cathode candidates for LT-SOFCs are indicated to possess excellent mixed ionic and electronic conductivity (MIEC). Such mixed conductivity can effectively extend the reaction zones for ORR from the triple phase boundaries (TPB) to the entire surface of cathode materials in contrast with singly electronic conductor.[10] As a desirable parent compound, $SrCoO_{3-\delta}$ (SC) has inspired substantial attention due to its high oxygen vacancy concentration and superior redox capability of Co ions.[11,12] In order to improve the structural stability of perovskite SC, numerous SC-based perovskites have been evolved by introducing various A-site and/or B-site substituting elements, such as $La_xSr_{1-x}Co_{1-y}Fe_yO_{3-\delta}$ (LSCF),[13,14] $Sm_xSr_{1-x}CoO_{3-\delta}$,[15,16] $SrCo_{1-x}Nb_xO_{3-\delta}$,[17,18] $Ba_xSr_{1-x}Co_{1-y}Fe_yO_{3-\delta}$.[19,20] These tuned perovskites can outperform conventional $LaMnO_3$-based cathode materials. Nevertheless, these materials tend to suffer from limited ionic conductivity and unsatisfactory stability at lower temperatures, which restrict their potential applications. For instance, a technical barrier for LSCF is its insufficient oxygen surface exchange and bulk diffusion properties at reduced temperatures.[21,22] As for $Ba_xSr_{1-x}Co_{1-y}Fe_yO_{3-\delta}$, a transformation (owing to larger Goldschmidt tolerance factor 1.052 over 1) from the cubic to hexagonal phase structure would take place below 800 °C and the degraded lattice geometric symmetry leads to a significant decline in conductivity and transport properties.[23,24]

As a feasible avenue, partial substitution of various ions has been employed to address the aforementioned shortcomings of SC-based cathode materials while maintaining adequate electrocatalytic performance at lower temperatures. Among the various B-site dopants, the relatively lower oxidation state and larger ionic radius have motivated the adoption of Ni ions as additional dopant for oxygen reduction electrodes.[25-31]

a. School of Chemical Engineering and Light Industry, Guangdong University of Technology, Guangzhou Higher Education Mega Center, Guangzhou 510006, China. E-mail: dongff@gdut.edu.cn; zhanlin@gdut.edu.cn; Tel: +86 20 39320229

b. Building Energy Research Group, Department of Building and Real Estate, The Hong Kong Polytechnic University, Hung Hom, Kowloon, Hong Kong 999077, China.

c. State Key Laboratory of Materials-Oriented Chemical Engineering, College of Chemical Engineering, Nanjing Tech University, No. 30 Puzhu South Road, Nanjing 211816, China.

† Electronic Supplementary Information (ESI) available. See DOI: 10.1039/x0xx00000x

Consequently, enhanced oxygen vacancy generation capability (charge conservation) and well-preserved perovskite structure (Goldschmidt tolerance factor and spin state equilibrium) would be beneficial to improving the electrocatalytic activity and stability. Recently, Longo et al. demonstrated that B-site Ni dopant in LSCF favored the stabilization of the oxygen vacancies and TM-O_6 structural units, resulting in maintained redox properties and improved ORR over a wide temperature range.[29] Additionally, Wang et al. reported the effect of Ni substitution on microstructural, mechanical and sintering behaviors of $Ba_{0.5}Sr_{0.5}Co_{0.8}Fe_{0.2}O_{3-\delta}$ (BSCF) oxygen transport membranes, which in turn affect oxygen activation properties.[30,31] Nevertheless, few studies are available on the effects of Ni co-dopant in BSCF system on the crystal structure and oxygen transport for catalyzing the ORR in LT-SOFCs cathodes.

Motivated by the aforementioned progressive research on oxygen activation, herein, we reported a newly developed perovskite oxide, Ni co-doped $Ba_{0.5}Sr_{0.5}Co_{0.7}Fe_{0.2}Ni_{0.1}O_{3-\delta}$ (BSCFN) as an oxygen reduction electrode for LT-SOFCs, with a focus on some fundamental features including the crystal structure, oxygen non-stoichiometry, and oxygen transport coefficients. A symmetrical cell with $Sm_{0.2}Ce_{0.8}O_{1.9}$ (SDC) electrolyte exhibits a low polarization resistance for BSCFN electrode, e.g. ~0.03 Ω cm^2 at 600 °C. Single cells with BSCFN cathode, conventional SDC thin-film electrolyte, and Ni-SDC anode-support yield excellent performance of ~1.8 W cm^{-2} at 650 °C. In addition, the electrode activity of BSCFN under open circuit conditions was examined to determine the long-term durability. Overall, the results show that Ni used as co-dopant can make for an optimized collocation of phase structure, oxygen vacancies, and oxygen-ion mobility at reduced temperatures, highlighting BSCFN as a highly desirable oxygen electrode for LT-SOFCs.

Experimental

Powder preparation

$Ba_{0.5}Sr_{0.5}Co_{0.7}Fe_{0.2}Ni_{0.1}O_{3-\delta}$ (BSCFN) powder was synthesized by a combined EDTA-citric acid complexing sol-gel method. Analytically-pure reagents $Ba(NO_3)_2$, $Sr(NO_3)_2$, $Co(NO_3)_2 \cdot 6H_2O$, $Fe(NO_3)_3 \cdot 9H_2O$ and $Ni(NO_3)_2 \cdot 6H_2O$ (all from Sinopharm Chemical Reagent) were weighed with stoichiometric ratio and dissolved in deionized water to form a homogeneous solution. Ethylenediaminetetraacetic acid (EDTA) and citric acid (CA), served as complexing agents, were added in sequence into the above solution. $NH_3 \cdot H_2O$ was used to adjust the pH of the solution to around 6. A transparent gel was obtained after continuous heating and stirring. This gel was then sent to an air oven and heated at 250 °C for at least 5 h, resulting in a black solid precursor. The precursor was calcined in air at 900 °C for 5 h to form fine BSCFN powder.

Cell fabrication

For a BSCFN|SDC|BSCFN symmetrical cell, a dense SDC substrate was first prepared by uniaxially pressing commercially available SDC (Fuelcell Materials) powder into a circular pellet and subsequently calcining at 1350 °C for 5 h. BSCFN powder

was uniformly dispersed in a mixed solution of isopropyl alcohol, ethylene glycol, and glycerol to form a colloidal suspension through ball-milling (Fritsch, Pulverisette 6) for 0.5 h. Then the colloidal suspension was deposited on both sides of the SDC pellet by a particle suspension spraying process. A symmetrical cell with porous BSCFN electrodes (~16 μm in thickness) was obtained after co-firing the pellet in air at 1000 °C for 2 h. Silver paste and attached silver wires served as current collector and leads, respectively.

Anode-supported single cells with NiO-SDC|SDC|BSCFN configuration were fabricated via dry-pressing and co-sintering processes. The NiO-SDC composite anode was first fabricated via ball-milling NiO, SDC, and polyvinyl butyral (PVB, acting as pore former) powders in a weight ratio of 6: 4: 0.8 in absolute ethanol for about 1 h. The composite powder was mechanically pressed into discs under 0.2 M pressure for 1-2 min after drying. An SDC electrolyte film was subsequently sprinkled onto the anode substrate via a co-pressed method followed by co-calcining at 1350 °C for 5 h. The thickness of electrolyte layer of the half-cell was 10-15 μm. Afterwards, the BSCFN cathode slurry was sprayed onto the SDC electrolyte using the same process for fabricating the symmetrical cell, followed by sintering at 1000 °C for 2 h to obtain a single cell.

Additional characterizations

X-ray diffraction (XRD, Rigaku MiniFlex600) with Cu Kα radiation (λ = 1.54059 Å) was used to detect the crystal structures of fresh and heat-treated (in ambient air under 600 °C for 200 h) samples. The diffraction patterns were recorded at room temperature by stepwise scanning (0.02° per step) over the range from 20° to 80°. To get more detailed structural information, Rietveld refinement of XRD pattern was carried out using General Structure Analysis System (GSAS) software with the EXPGUI interface.[32] The microstructure and crystallinity of BSCFN powder were determined by transmission electron microscope (TEM, Talos F200S) equipped with energy-dispersive X-ray (EDX). The oxygen non-stoichiometries of BSCFN sample at different temperatures were quantified through combining iodometric titration method and thermo-gravimetric analysis (TGA, Netzsch, TG 209 F3), with detailed experimental procedures described before.[33] For electrical conductivity measurement of the investigated specimens, bar-shaped dense samples with geometric dimensions of ~2 mm × 5 mm × 12 mm were prepared by dry pressing with subsequent calcination of 1150 °C for 5 h. The sample was then tested by four-probe DC method using Keithley 2420 source meter within the temperature range of 400-800 °C at intervals of 10 °C. The dense bar-shaped sample can be also used to determine the oxygen kinetics (e.g. surface exchange coefficient (k_{chem}) and bulk diffusion coefficient (D_{chem})) with the electrical conductivity relaxation (ECR) technique. The ECR process, conducted between 450 and 650 °C with 50 °C incremental steps, was realized by suddenly changing the oxygen partial pressure from 0.1 to 0.21 atm once the bar reached an equilibrium state, leading to the corresponding changes in the electrical conductivity. The transient thermogravimetric method was used to detect the kinetics of oxygen conduction. The program

was as follows: approximately 10 mg pre-treated BSCFN powder was heated from room temperature to 600 °C with a heating rate of 10 °C min^{-1} in pure argon and kept at 600 °C for 1 h; subsequently, the atmosphere was swiftly changed to air and held for another hour with the temperature unchanged, till the end of the program. The flowing rate of the gases was 50 mL min^{-1}.

Electrochemical characterization

The electrode polarization resistance of the symmetrical cell was measured in air using a Solartron 1287 potentiostat and a Solartron 1260 frequency response analyzer with the testing temperature ranged from 450 to 650 °C. The measurement was under open circuit voltage (OCV) conditions with the applied frequency range from 100 kHz to 0.1 Hz and the potential amplitude was 10 mV. *I-V* and *I-P* polarization tests were used to assess the performance of button single cells at the operating temperatures of 450-650 °C, which can be implemented by a Keithley 2420 Source Meter with a four-probe configuration. The single cell was mounted on a quartz tube with silver paste (DAD87, Shanghai Research Institute for Synthetic Resins) for fuel cell test. Moist H$_2$ (~3% H$_2$O) with a fixed flow rate of 80 mL min^{-1} was fed as fuel for anode side while ambient air served as oxidant for cathode side.

Results and discussion

Crystal structure

The crystal structure of perovskite encompasses a wide array of physicochemical properties, with a close affiliation with electrocatalytic activity in electrochemical conversion devices. The typical XRD pattern from BSCFN powder shown in Fig. 1 exhibits only characteristic peaks of the perovskite structure, identifying a single well-formed perovskite framework without any detectable secondary phases. To gain the quantitative information of crystal structure, Rietveld refinement was conducted on the XRD data with the crystallographic details shown in the inset of Fig. 1 and Table S1. It is revealed that the XRD pattern could be assigned to a cubic symmetrical structure
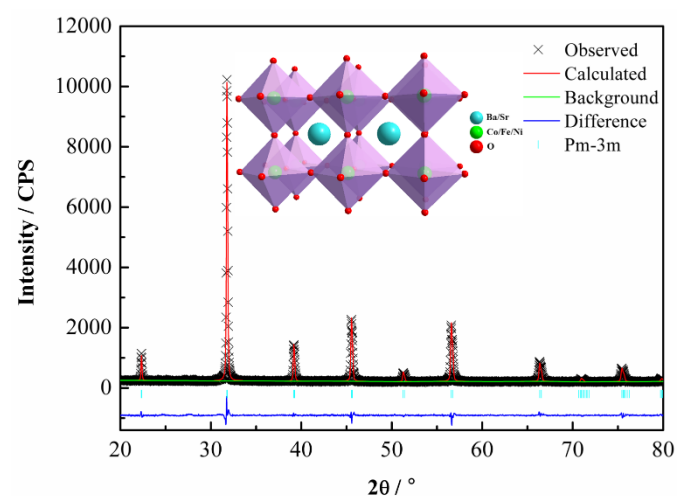
with $Pm\overline{3}m$ space group and a lattice constant of 3.9815 Å. A good fit was achieved between calculated profile and observed pattern and high reliability of structural model was validated by desirable refinement factors of weighted pattern R_{wp} = 5.88%, pattern R_p = 4.47%, and goodness of fit χ^2 = 0.977.

A slight expansion of lattice parameter was observed for the sample BSCFN relative to BSCF,[34] due to the marginally larger ionic radius of Ni over Co, providing further evidence for Ni incorporation into the perovskite lattice as a substitution. The Goldschmidt tolerance factor of BSCFN can be tuned closer to 1 by substituting larger Ni ions into the B-site, rationalizing the structural stability. Accordingly, when post-annealed at 600 °C in ambient air for 200 h, the cubic perovskite structure was preserved, as embodied by the inconspicuous change of the main perovskite XRD peaks (Fig. S1), suggesting that the synthesized sample manifested superior structural stability. Moreover, to demonstrate the desirable cubic-symmetry structural stability of BSCFN at elevated temperatures, the as-prepared sample was further subjected to high temperature XRD (HT-XRD) analysis. Fig. S2 shows the HT-XRD patterns of BSCFN powder between room temperature and 700 °C in air, measured by step increase of the temperature at a rate of 5 °C min^{-1} and then a reverse step decrease to room temperature. It was found that the BSCFN sample retained its perovskite lattice structure at high temperatures, since no obvious phase transition or additional peak was observed in both heating and cooling processes, suggesting the thermodynamically stable cubic-symmetry perovskite structure of the BSCFN oxide at elevated temperatures.

Furthermore, to acquire deeper insight into the microstructure and crystallinity of BSCFN, we employed high-resolution TEM (HRTEM) in combination with elemental mapping using the EDX of powder morphology. The enlarged HRTEM image from the region outlined by a red dotted rectangle in Fig. 2a reveals that the periodic spacing of crystalline fringes is ~0.285 nm, as
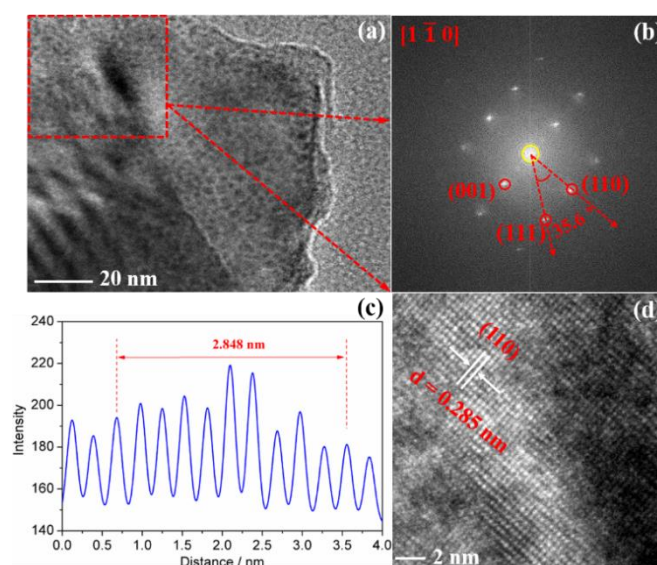

Fig. 2 Crystalline structure of BSCFN. (a) HRTEM image of the BSCFN lattice; (b) corresponding FFT patterns, (c) intensity profile of crystalline fringes and (d) emerging lattice fringes of magnified view in the selected region in (a).

Fig. 1 Refined XRD profiles of BSCFN powder after firing in air at 900 °C for 5 h. The inset is the schematics of the crystal structure.

marked in Fig. 2d, which is close to that of (110) plane of perovskite structure with cubic symmetry from XRD refinement results. The spacing is also verified by the intensity distribution of lattice fringes as plotted in Fig. 2c. The corresponding fast Fourier transformation (FFT) patterns can be consistently indexed as a cubic perovskite crystal viewed along the $[1\bar{1}0]$ zone axis, which is supported by the distance of (001), (110), and (111) planes, as well as the included angle (35.6º) (Fig. 2b). The above results match well with the analysis of XRD, further confirming the cubic-symmetry perovskite structure of BSCFN sample. Moreover, in the elemental distribution by EDX mapping analysis taken from the region in the TEM image (Fig. S3), a uniform distribution without the segregation of all the elements (Ba, Sr, Co, Fe, and Ni) in BSCFN is clearly evident.

Oxygen transport

It is generally accepted that ORR catalytic activity is strongly associated with oxygen vacancy concentration in the perovskite structure, which can be facilely modified by substituting strategy. The oxygen nonstoichiometry of the investigated specimens at room temperature was determined by iodometric titration and TGA was performed to guide the evolution of oxygen vacancies at elevated temperatures, thus calculating the oxygen nonstoichiometry as a function of temperature. As shown in Fig. 3, the amount of oxygen vacancies formed in BSCFN oxide is roughly δ = 0.42-0.53 over the operating temperature range of 450-650 °C, which surpasses that of the counterpart BSCF perovskite as a well-known benchmark, as well as other prevailing perovskites.[35-37] The high level of oxygen vacancies indicates that the substitution of lower-valence Ni can contribute to the formation of more oxygen vacancies due to the electroneutrality maintenance. The generated oxygen vacancies are expected to provide more active sites for enhanced mobility and transferability of oxygen ions in the perovskite material.
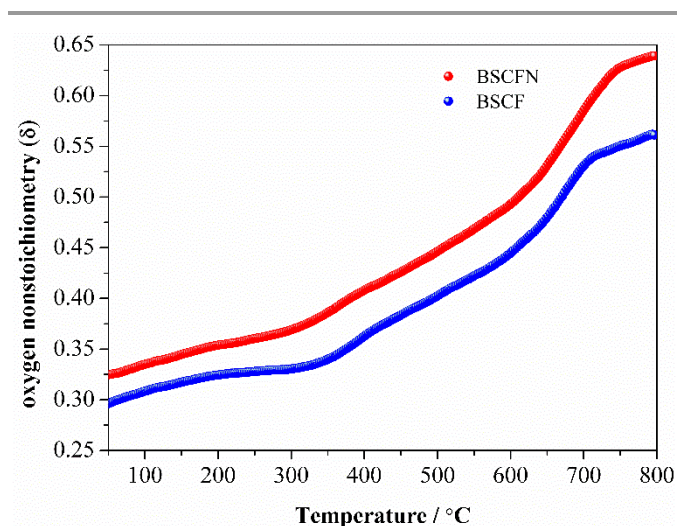
To further support the prominent oxygen kinetics for ORR, the rates of oxygen bulk and surface reactions were quantified with the chemical bulk diffusion coefficient (D_{chem}) and chemical surface exchange coefficient (k_{chem}), which were extracted from conductivity profiles using ECR method. The typical ECR profiles and the resulting D_{chem} and k_{chem} are plotted in Fig. 4 for BSCFN oxide. The favorable D_{chem} and k_{chem} values for BSCFN were obtained, which are approximately one order of magnitude larger than those for BSCF.[38] For example, at 600 °C, the D_{chem} and k_{chem} are 1.24×10^{-4} cm^2 s^{-1} and 1.32×10^{-3} cm s^{-1} for BSCFN, respectively; by contrast, the corresponding values are 2.5×10^{-5} cm^2 s^{-1} and 2.7×10^{-4} cm s^{-1} for BSCF, respectively. Our results strongly suggest that Ni substitution can significantly improve the oxygen activity in terms of bulk diffusion and surface exchange. From the temperature dependence of D_{chem} and k_{chem} in the Arrhenius-type plots, the as-obtained activation energies are 84.9 kJ mol^{-1} and 86.7 kJ mol^{-1}, respectively. The low activation energies are comparable to those of many prevalent perovskite oxides,[39,40] which is desirable for reduced-temperature operation.
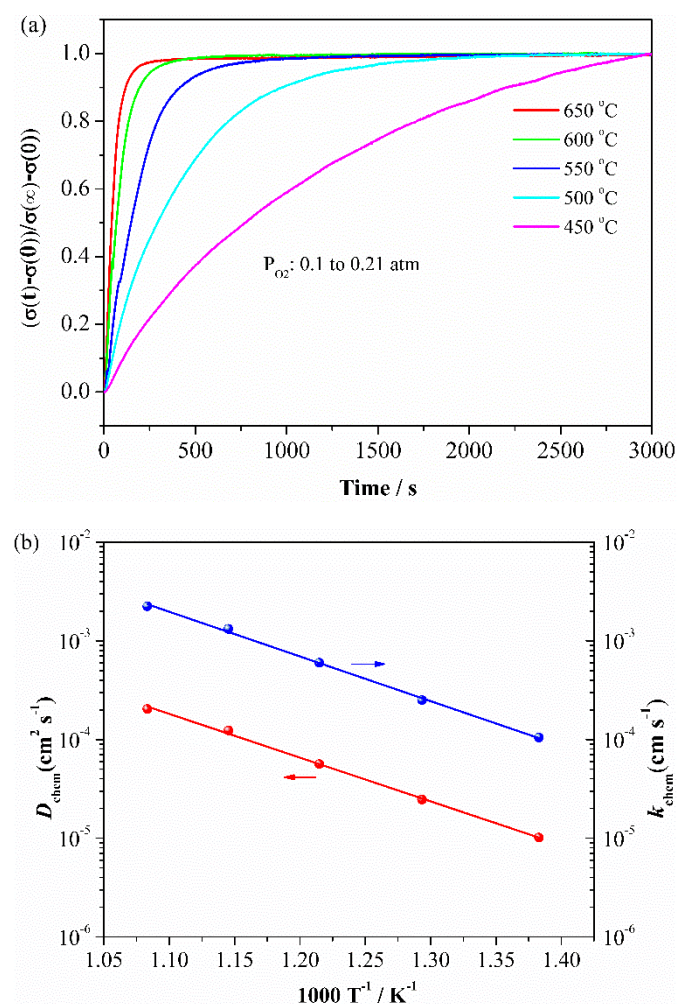
(a)

(b)

Fig. 4 (a) ECR response profiles of BSCFN at various temperatures after a swift change in oxygen partial pressure from 0.1 to 0.21 atm; (b) temperature dependence of the fitted D_{chem} and k_{chem}.

Fig. 3 Temperature dependence of the oxygen nonstoichiometry (δ) for BSCFN material with BSCF as a perovskite counterpart.

The fast oxygen kinetics was also verified by the transient thermogravimetric measurement, during which oxygen transport involved exchange on the grain surface and diffusion in the grain bulk. When switching the flow from argon to air, the BSCFN sample experienced a significant weight change in the adsorption period. It is observed from Fig. S4 that BSCFN takes a very short time (~3 min) for quick response to reach a new equilibrium, implying a fast oxygen surface exchange and bulk diffusion process. In addition to oxygen transport, the BSCFN also demonstrated acceptable electrical conductivity to provide paths for electron transfer within the operating temperature range (Fig. S5). Results from oxygen transport are conducive to the electrocatalytic performance of BSCFN perovskite oxide for ORR.

Electrochemical performance

To evaluate the electrochemical performance of BSCFN as oxygen electrodes, the symmetrical cells with a configuration of BSCFN|SDC|BSCFN were characterized by EIS measurement. Shown in Fig. 5a are the typical Nyquist plots of EIS data measured from 450 °C to 650 °C. The area-specific resistance (ASR) values of BSCFN electrode are determined by the difference between high- and low-frequency intercepts on the real axis in the Nyquist plot. The BSCFN electrode delivers a remarkable ORR activity at reduced temperatures, with ASRs as low as 0.63, 0.20, 0.076, 0.033, 0.018 Ω cm^2 at 450, 500, 550, 600 and 650 °C, respectively. The electrocatalytic activity of BSCFN cathode outperforms other BSCF-based cathode materials,[41-43] clearly indicating that Ni doping could effectively enhance the electroactivity. For instance, the ASR value of BSCFN is approximately 1/3 that of BSCF benchmark (~0.09 Ω cm^2) at 600 °C, and is also lower than that of La-doped BSCF (~0.06 Ω cm^2) and Y-doped BSCF (~0.07 Ω cm^2) at 600 °C. The detailed comparison of ASR values between BSCFN and other prevailing Co-based cathode compositions is summarized in Table 1. In addition, BSCFN shows a very low activation energy of 100.2 kJ mol^{-1}, calculated from the Arrhenius-type plot of ASRs in Fig. 5b, implying the maintained high-activity for ORR at low temperatures.
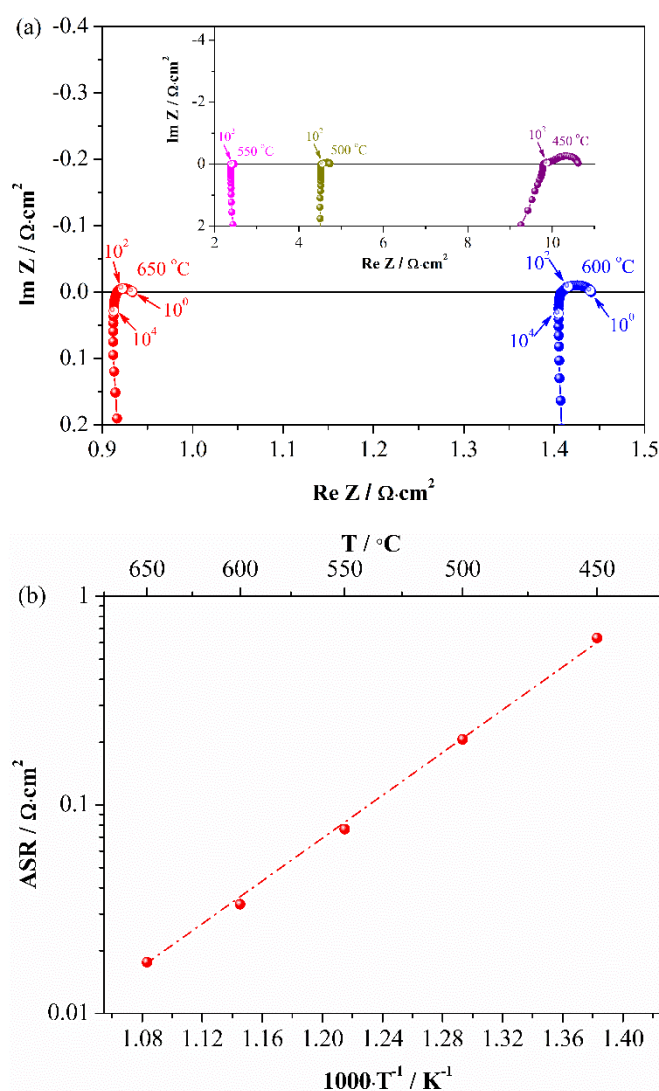

Fig. 5 (a) Nyquist-type and (b) Arrhenius-type plots of the BSCFN in a symmetrical cell as a function of temperature.

Table 1 Comparison of ASRs for different cobalt-based electrodes based on symmetrical cells

Electrode	Electrolyte	ASR (Ω cm^2) @600 °C	Ref.
$Sr_{0.95}Ag_{0.05}Nb_{0.1}Co_{0.9}O_{3-\delta}$	SDC	0.0374	44
$Sr_{0.95}Co_{0.8}Nb_{0.1}Ta_{0.1}O_{3-\delta}$	SDC	0.12	45
$SrSc_{0.175}Nb_{0.025}Co_{0.8}O_{3-\delta}$	SDC	0.04	39
$La_{0.6}Sr_{0.4}Co_{0.2}Fe_{0.7}Nb_{0.1}O_{3-\delta}$-$Er_{0.4}Bi_{1.6}O_3$	YSZ	7.2	46
$La_{0.6}Sr_{0.4}Co_{0.2}Fe_{0.8}O_{3-\delta}$-$Ce_{0.9}Gd_{0.1}O_{2-\delta}$-$La_{1-x}Sr_xCoO_{3-\delta}$	GDC	~0.11	47
$BaCoO_{3-x}$-$PrCoO_{3-x}$-$PrBa_{0.8}Ca_{0.2}Co_2O_{5+\delta}$	YSZ	~0.312	22
$PrBa_{0.8}Ca_{0.2}Co_2O_{5+\delta}$	SDC	~0.31	48
$PrBa_{0.5}Sr_{0.5}Co_2O_{5+\delta}$	SDC	0.109	8
$NdBa_{0.75}Ca_{0.25}Co_2O_{5+\delta}$	GDC	0.066	6
BSCF	SDC	0.093	41
$La_{0.5}Ba_{0.25}Sr_{0.25}Co_{0.8}Fe_{0.2}O_{3-\delta}$-GDC	GDC	0.064	42
$(Ba_{0.5}Sr_{0.5})(Co_{0.8}Fe_{0.2})_{0.9}Y_{0.1}O_{3-\delta}$	GDC	0.070	43
$Ba_{0.5}Sr_{0.5}(Co_{0.7}Fe_{0.3})_{0.6875}W_{0.3125}O_{3-\delta}$	SDC	~0.1	49
BSCF-GDC	GDC	0.224	50
BSCFN	**SDC**	**0.033**	**This work**

SDC: $Sm_{0.2}Ce_{0.8}O_{1.9}$; GDC: $Gd_{0.1}Ce_{0.9}O_{1.95}$; YSZ: $Y_{0.16}Zr_{0.92}O_{2.0}$
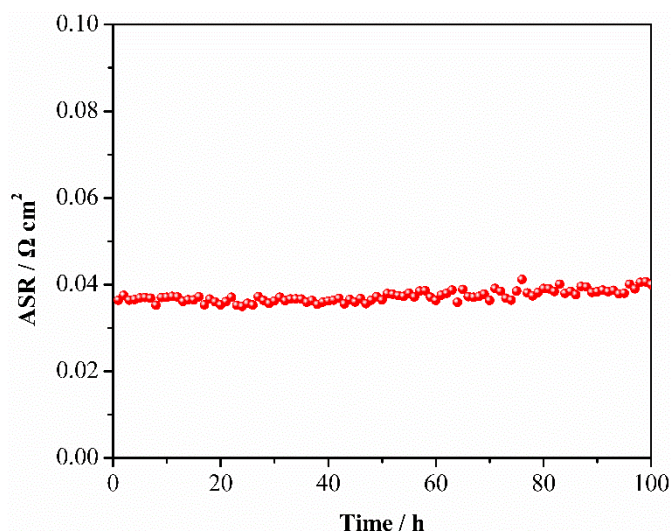
Fig. 6 Durability of the BSCFN sample at 600 °C in air under OCV conditions.

Apart from high electrocatalytic activity, durability is a vital factor determining the practical application of cathode materials. Accordingly, ~100 h of long-term stability test was carried out on BSCFN-electrode symmetrical cells at 600 °C. As shown in Fig. 6, the polarization resistance of BSCFN remained stable within the measurement accuracy during the durability test, which could be attributed to the maintained perovskite structure without the appearance of impurity phases. As depicted in Fig. S6, when exposed to air containing high-level concentration of CO_2 (10 vol.%), it is clear that the electrocatalytic activity of the BSCFN electrode was degraded significantly with time. In spite of this, the polarization resistance rapidly recovered close to the original value after switching to pure air gas, suggesting the reversible effect of CO_2 with high concentration.

To further evaluate the electrochemical performance of BSCFN cathode in an actual fuel cell, the anode-supported cells with a configuration of Ni-SDC|SDC|BSCFN were fabricated and subjected to *I-V* measurement with the *I-V-P* curves exhibited in Fig. 7. The maximum power densities as high as 149, 345, 745, 1317, and 1816 mW cm^{-2} could be achieved at 450, 500, 550,
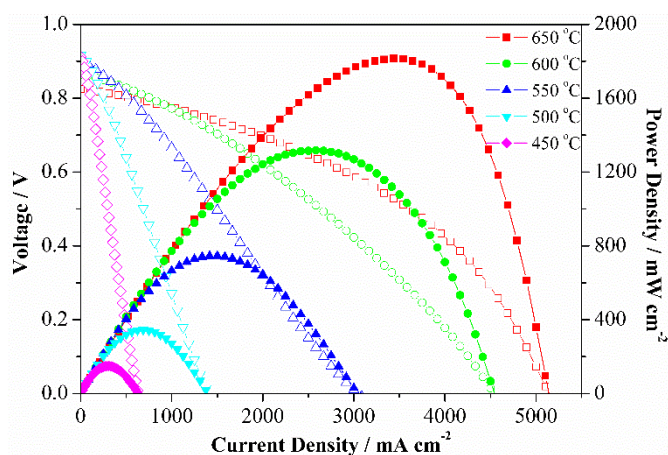

Fig. 7 Typical *I-V-P* curves of a single cell with BSCFN cathode measured at temperatures of 450-650 °C.

600 and 650 °C, respectively, which are higher than those of the single cell with the BSCF cathode and comparable to the outstanding performance ever reported (Table S2), suggesting superior electrocatalytic activity of the BSCFN cathode under practical operating conditions. Taking into consideration the ease and routinization of fabrication processes in single cells, the preliminary results on electrochemical performance are expected to be noticeably improved through the advanced thin-film technology and microstructure (porosity) optimization for electrolyte and anode processing, respectively.

Conclusions

In summary, a perovskite composition $Ba_{0.5}Sr_{0.5}Co_{0.7}Fe_{0.2}Ni_{0.1}O_{3-\delta}$ (BSCFN) has been fabricated and evaluated as an oxygen reduction electrode for reduced-temperature SOFCs. Endowed with a preserved cubic-symmetry phase structure, the BSCFN catalyst exhibits high oxygen vacancy concentration in conjunction with fast oxygen incorporation and diffusion kinetics, enabling superior electrochemical activity for ORR. The ASR values of only ~0.033 and ~0.20 Ω cm^2 are achieved at 600 and 500 °C, respectively, in a symmetrical cell configuration, thus high power output of BSCFN-derived single fuel cell. The substantial enhancement margin over BSCF is accomplished owing to the substitution of Ni for B-site, contributing to the advancement for LT-SOFCs community. Furthermore, on the basis of the favorable activity and durability for oxygen catalysis, the developed BSCFN-based perovskite materials may be applicable to other catalytic and electrochemical processes, including solid oxide electrolysis cells, oxygen pumps, oxygen sensors, and oxygen permeable membranes.

Conflicts of interest

There are no conflicts to declare.

Acknowledgements

Notes and references

1   S. Park, J.M. Vohs and R.J. Gorte, *Nature*, 2000, **404**, 265–267.
2   R. M. Ormerod, *Chem. Soc. Rev.*, 2003, **32**, 17-28.
3   C. Duan, R. J. Kee, H. Zhu, C. Karakaya, Y. Chen, S. Ricote, A. Jarry, E. J. Crumlin, D. Hook, R. Braun, N. P. Sullivan and R. O'Hayre, *Nature*, 2018, **557**, 217-222.
4   E. D. Wachsman and K. T. Lee, *Science*, 2011, **334**, 935–939.
5   W. He, X. Wu, G. Yang, H. Shi, F. Dong and M. Ni, *ACS Energy Lett.*, 2017, **2**, 301-305.
6   S. Yoo, A. Jun, Y. W. Ju, D. Odkhuu, J. Hyodo, H. Y. Jeong, N. Park, J. Shin, T. Ishihara and G. Kim, *Angew. Chem., Int. Ed.*, 2014, **53**, 13064-13067.

7   C. Duan, J. Tong, M. Shang, S. Nikodemski, M. Sanders, S. Ricote, A. Almansoori and R. O'Hayre, *Science*, 2015, **349**, 1321–1326.
8   Y. Chen, Y. Bu, B. Zhao, Y. Zhang, D. Ding, R. Hu, T. Wei, B. Rainwater, Y. Ding, F. Chen, C. Yang, J. Liu and M. Liu, *Nano Energy*, 2016, **26**, 90-99.
9   M. Li, M. Zhao, F. Li, W. Zhou, V. K. Peterson, X. Xu, Z. Shao, I. Gentle and Z. Zhu, *Nat. Commun.*, 2017, **8**, 13990.
10 S. B. Adler, *Chem. Rev.*, 2004, **104**, 4791–4843.
11 V. V. Vashook, M. V. Zinkevich and Y. G. Zonov, *Solid State Ionics*, 1999, **116**, 129–138.
12 Z. Q. Deng, W. S. Yang, W. Liu and C. S. Chen, *J. Solid State Chem.*, 2006, **179**, 362-369.
13 A. Esquirol, N. P. Brandon, J. A. Kilner and M. Mogensen, *J. Electrochem. Soc.*, 2004, **151**, A1847 -A1855.
14 D. Oh, D. Gostovic and E. D. Wachsman, *J. Mater. Res.*, 2012, **27**, 1992-1999.
15 C. Xia, W. Rauch, F. Chen and M. Liu, *Solid State Ionics*, 2002, **149**, 11–19.
16 F. Dong, D. Chen, R. Ran, H. Park, C. Kwak and Z. Shao, *Int. J. Hydrogen Energy*, 2012, **37**, 4377-4387.
17 F. Wang, Q. Zhou, T. He, G. Li and H. Ding, *J. Power Sources*, 2010, **195**, 3772-3778.
18 M. Li, W. Zhou, V. K. Peterson, M. Zhao and Z. Zhu, *J. Mater. Chem. A*, 2015, **3**, 24064-24070.
19 Z. Shao and S. M. Haile, *Nature*, 2004, **431**, 170–174.
20 W. Zhou, R. Ran and Z. Shao, *J. Power Sources*, 2009, **192**, 231-246.
21 C. Endler-Schuck, J. Joos, C. Niedrig, A. Weber and E. Ivers-Tiffée, *Solid State Ionics*, 2015, **269**, 67-79.
22 Y. Chen, Y. Choi, S. Yoo, Y. Ding, R. Yan, K. Pei, C. Qu, L. Zhang, I. Chang, B. Zhao, Y. Zhang, H. Chen, Y. Chen, C. Yang, B. deGlee, R. Murphy, J. Liu and M. Liu, *Joule*, 2018, **2**, 938-949.
23 S. Švarcová, K. Wiik, J. Tolchard, H.J.M. Bouwmeester and T. Grande, *Solid State Ionics*, 2008, **178**, 1787-1791.
24 C. Niedrig, S. Taufall, M. Burriel, W. Menesklou, S. F. Wagner, S. Baumann and E. Ivers-Tiffée, *Solid State Ionics*, 2011, **197**, 25-31.
25 P. Hjalmarsson, M. Søgaard and M. Mogensen, *Solid State Ionics*, 2009, **180**, 1395-1405.
26 Y.-P. Fu, *Int. J. Hydrogen Energy*, 2010, **35**, 8663-8669.
27 E. G. Babakhani, J. Towfighi, L. Shirazi, A. Nakhaeipour, A. Zamaniyan and Z. Shafiei, *J. Mater. Sci. Technol.*, 2012, **28**, 177-183.
28 Y.-P. Fu, A. Subardi, M.-Y. Hsieh, W.-K. Chang and J. Stevenson, *J. Am. Ceram. Soc.*, 2016, **99**, 1345-1352.
29 A. Longo, L. F. Liotta, D. Banerjee, V. La Parola, F. Puleo, C. Cavallari, C. J. Sahle, M. Moretti Sala and A. Martorana, *J. Phys. Chem. C*, 2018, **122**, 1003-1013.
30 L. Wang, R. Dou, Y. Li, H. Lu, M. Bai, D. Hall and Y. Chen, *Mater. Sci. Eng. A*, 2016, **658**, 280-288.
31 L. Wang, Y. Chen, G. Wang, Y. Li, M. Bai, D. Hall and R. Dou, *Adv. Appl. Ceram.*, 2018, **117**, 269-278.
32 B. H. Toby, *J. Appl. Crystallogr.*, 2001, **34**, 210–213.
33 F. Dong, Y. Chen, D. Chen and Z. Shao, *ACS Appl. Mater. Interfaces*, 2014, **6**, 11180-11189.
34 U. P. Azad, M. Singh, S. Ghosh, A. K. Singh, V. Ganesan, A. K. Singh and R. Prakash, *Int. J. Hydrogen Energy*, 2018, **43**, 20671-20679.
35 Y. Zhu, Z. G. Chen, W. Zhou, S. Jiang, J. Zou and Z. Shao, *ChemSusChem*, 2013, **6**, 2249-2254.
36 F. Dong, M. Ni, W. He, Y. Chen, G. Yang, D. Chen and Z. Shao, *J. Power Sources*, 2016, **326**, 459-465.
37 T. Yang, A. H. Matthews, N. Xu, Y. Chen, K. An, D. Ma and K. Huang, *ACS Appl. Mater. Interfaces*, 2018, **10**, 35984-35993.
38 D. Chen and Z. Shao, *Int. J. Hydrogen Energy*, 2011, **36**, 6948-6956.
39 W. Zhou, J. Sunarso, M. Zhao, F. Liang, T. Klande and A. Feldhoff, *Angew. Chem., Int. Ed.*, 2013, **52**, 14036-14040.
40 F. Dong, M. Ni, Y. Chen, D. Chen, M. O. Tadé and Z. Shao, *J. Mater. Chem. A*, 2014, **2**, 20520-20529.
41 W. Zhou, R. Ran, Z. Shao, W. Zhuang, J. Jia, H. Gu, W. Jin and N. Xu, *Acta Mater.*, 2008, **56**, 2687-2698.
42 J. Kim, S. Choi, A. Jun, H. Y. Jeong, J. Shin and G. Kim, *ChemSusChem*, 2014, **7**, 1669-1675.
43 L. Almar, H. Störmer, M. Meffert, J. Szász, F. Wankmüller, D. Gerthsen and E. Ivers-Tiffée, *ACS Appl. Energy Mater.*, 2018, **1**, 1316-1327.
44 Y. Zhu, W. Zhou, R. Ran, Y. Chen, Z. Shao and M. Liu, *Nano Lett.*, 2016, **16**, 512-518.
45 X. Ding, Z. Gao, D. Ding, X. Zhao, H. Hou, S. Zhang and G. Yuan, *Appl. Catal. B Environ.*, 2019, **243**, 546-555.
46 S. He, Q. Zhang, G. Maurizio, L. Catellani, K. Chen, Q. Chang, M. Santarelli and S. P. Jiang, *ACS Appl. Mater. Interfaces*, 2018, **10**, 40549-40559.
47 Y.-L. Huang, A. M. Hussain and E. D. Wachsman, *Nano Energy*, 2018, **49**, 186-192.
48 Y. Chen, S. Yoo, Y. Choi, J. H. Kim, Y. Ding, K. Pei, R. Murphy, Y. Zhang, B. Zhao, W. Zhang, H. Chen, Y. Chen, W. Yuan, C. Yang and M. Liu, *Energy Environ. Sci.*, 2018, **11**, 2458-2466.
49 J. F. Shin, W. Xu, M. Zanella, K. Dawson, S. N. Savvin, J. B. Claridge and M. J. Rosseinsky, *Nat. Energy*, 2017, **2**, 1-7.
50 J. G. Lee, J. H. Park and Y. G. Shul, *Nat. Commun.*, 2014, **5**, 4045.